Author/s:
Russell, BJ;Balendhran, S;Meng, J;Crozier, KB

Title:
Thermo-Optically Tunable Mid-Infrared Bandpass Filters Comprising Ultra-Thin Silicon-on-Sapphire Metasurfaces

Date:
2025-11-06

Citation:
Russell, B. J., Balendhran, S., Meng, J. & Crozier, K. B. (2025). Thermo-Optically Tunable Mid-Infrared Bandpass Filters Comprising Ultra-Thin Silicon-on-Sapphire Metasurfaces. Laser and Photonics Reviews, 19 (21), https://doi.org/10.1002/lpor.202400853.

Persistent Link:
https://hdl.handle.net/11343/362572

LASER & PHOTONICS REVIEWS
www.lpr-journal.org

Thermo-Optically Tunable Mid-Infrared Bandpass Filters Comprising Ultra-Thin Silicon-on-Sapphire Metasurfaces

*Benjamin J. Russell, Sivacarendran Balendhran, Jiajun Meng, and Kenneth B. Crozier**

There is a need for high performance and compact mid-infrared hyperspectral imaging and spectroscopy systems for the reliable optical detection of chemical contaminants in environmental science, agriculture, heavy industry, and defense contexts. These applications are traditionally serviced by Fourier transform infrared (FTIR) spectrometers, but such systems are large, heavy, power hungry and of high cost. Tunable bandpass filters present a means to achieve mid-infrared spectrometers that are very compact, but previous approaches based on microelectromechanical systems are hindered by complex fabrication methods. Herein, how the thermo-optic effect can be exploited in zero-contrast grating (ZCG) based filters to create tunable filters for optical sensing applications that are solid state and narrowband is shown. Thermo-optically tunable mid-infrared bandpass filters are fabricated with center wavelengths around 3.45 µm based on one and two-dimensional ZCGs. It is showed that the center wavelength of the passband can be tuned up to 141 nm by varying the temperature (by 780 K), which exceeds the full-width-at-half-maximum of the passband (29 nm). It is demonstrated that the application of these devices to mid-infrared spectral reconstruction of the transmittance of several IR-transparent samples.

1. Introduction

Bandpass filters (BPFs) are useful tools for chemical sensing. In the non-dispersive infrared (NDIR) sensing paradigm, a broadband light source is filtered by a BPF with a passband matched to an absorption line of the gas nominated for detection. The filtered light passes through an analysis volume, and onto a photodetector, producing a signal. Variations of the target gas concentration in the analysis volume produce a corresponding variation in signal intensity, that, given prior calibration of the system, can be used to infer the gas concentration. Several systems have been conceived that utilize NDIR sensing methods for gas sensing.[1–4] Furthermore, well-characterized NDIR sensing systems that feature multiple filtering channels can be extended to spectral reconstruction functionalities.[5–8]

BPFs have also been integrated with sensing technologies that include photoacoustic spectrometers and infrared bolometer arrays.[9,10] Linear variable filtering is a mature technology that enables bandpass filtering with a tunable center wavelength at the expense of a few compromises; the requisite distributed Bragg reflectors (DBRs) require accurate deposition of alternating material layers, they are bandwidth-limited to one free spectral range, they require wedged spacers to manifest a varying cavity thickness, and they achieve tuning through mechanical means.[11,12] Micro-electromechanical systems vary this cavity thickness by actuating one of the DBRs.[13,14] To circumvent the shortcomings associated with these methods, we instead realize monolithically patterned filters with fabrication processes that are reliable and scalable. Metasurfaces are particularly capable as spectral BPFs, and their utility can be amplified by incorporating a tuning modality, enabling hyperspectral imaging and molecular fingerprinting. This tunability can be accessed through a number of distinct mechanisms. Mechanical methods include varying the angle of incidence, stretching an elastic substrate to vary scatterer pitch, and adjusting the relative lattice angle of interfaced metasurfaces.[5,15–21]

Devices that can be tuned devices optoelectronically instead of mechanically are inherently more integrable, stable, and miniaturizable. Typical OE methods include liquid crystal superstrates and field-effect modulation.[22–26] Tuning enabled by electrochromic materials, phase-change and materials (PCMs), and the thermo-optic (TO) effect have also garnered considerable interest in recent years.[27–37] Germanium-antimony-tellurium (GST), a PCM, elicits index shifts via a phase transformation that is dependent on annealing temperature. GST has been used to produce mid-infrared (MIR) transmission BPFs with a cen-

B. J. Russell, S. Balendhran, J. Meng, K. B. Crozier
School of Physics, The University of Melbourne
Parkville, Victoria 3010, Australia
E-mail: Kcrozier@unimelb.edu.au
B. J. Russell, J. Meng, K. B. Crozier
ARC Centre of Excellence for Transformative Meta-optical Systems (TMOS)
The University of Melbourne
Parkville, Victoria 3010, Australia
S. Balendhran, K. B. Crozier
Department of Electrical and Electronic Engineering
The University of Melbourne
Parkville, Victoria 3010, Australia

The ORCID identification number(s) for the author(s) of this article can be found under https://doi.org/10.1002/lpor.202400853

DOI: 10.1002/lpor.202400853

ter wavelength that can be modulated with subsequent annealing in a vacuum chamber or with nanosecond laser pulses.[38,39] The TO effect presents an alternative means to precisely and reliably tune refractive index, that can be done in situ.[40,41] It originates from free carrier ionization and thermal expansion[42] and is perpetually reversible. The maturity of crystalline silicon (c-Si) processing reflects its ubiquity in the electronics industry. The optical properties of c-Si films are known precisely, and, in contrast to many emerging PCMs, are largely independent of the processing conditions. c-Si also possesses a remarkably high TO coefficient ($\frac{dn}{dT}$) throughout the visible and infrared bands, which has made it a strong candidate for tunable metasurfaces for a variety of applications that include switchable pixels, filters, beam steerers, polarizers, but not a transmission BPF as of yet.[28–36,40,41,43,44] Methods of driving TO tuning are similarly varied, and typically employ integrated Joule microheaters or cryogenic-capable thermal stages.[28,30,40,41,45] Additionally, in an appropriately designed metasurface, the photothermal effect can enable all-optically driven TO tuning.[43,44]

The challenge is therefore creating an ideal MIR transmission BPF: one that is highly spectrally selective, compact, robust, easily fabricable, and tunable. We consider a class of coupled grating-waveguide based filters known as zero-contrast gratings (ZCGs), named for the vanishing index contrast between the waveguide and grating layers. ZCGs are a subset of resonant waveguide gratings, which are known for their propensity to support various local and non-local resonant phenomena, which can be exploited to mimic the function of free space optical elements such as beam-splitters, filters, mirrors, and polarizers.[46–54] Of particular note are demonstrations by M. J. Uddin and R. Magnusson of limited TO tuning of a bandpass feature in the near-infrared reflection spectrum of a ZCG in ref. [41]. Herein we have designed, fabricated, and characterized MIR transmission BPFs based on a silicon on sapphire (SoS) fabrication process. We have optimized ZCG filters for selective passbands, fabricated them using standard methods of lithography, evaporation, and etching, and characterized the temperature dependence of the spectral positions of the passband positions in simulation and in experiment. We produce filters that exhibit reliable tuning characteristics that are faithful to simulation by taking advantage of standard silicon processing techniques. To the best of our knowledge, this work represents the first demonstration of a tunable, MIR transmission bandpass filter where tuning is non-mechanical and is done in-situ. Furthermore, we apply this thermal tuning mechanism to the MIR spectral reconstruction of several semi-transparent samples.

2. Filter Design

In subwavelength ZCGs, broad transmission stopbands can be achieved through the efficient coupling between diffracted modes produced by the patterned grating layer and guided modes in the waveguide layer.[55] Simultaneously, transmission resonances can be engineered via quasi bound-states-in-the-continuum (qBICs), and evanescent cavity modes in the grating and waveguide layers.[56,57] The concurrence of these phenomena allows the creation of spectrally selective BPFs. These ZCGs typically employ high index materials such as silicon and germanium, which have notably high TO coefficients with respect to other dielectrics.[42] However, chalcogenides such as PbTe can possess an anomalously large, and negative, TO coefficient, which has enabled ultra-wide tuning over exceptionally narrow temperature ranges, as well as temperature invariant metasurfaces.[45,58] The substrates on which our Si films are formed require certain attributes in order to realize TO-tuned MIR filters. These include a high thermal conductivity to transfer heat to and from the gratings, weak MIR absorption to limit attenuation in transmission, and a low refractive index compared to the material from which the ZCG is formed (e.g., silicon). Sapphire ($\alpha - Al_2O_3$) meets these criteria.[59] We therefore procured S wafers (supplier: University Wafer) with a specified Si films thickness of $t = 1.5 \pm 0.15$ μm.[60]

For the 1D ZCG (**Figure 1a**), we targeted broadband extinction at normal incidence and relied on the manifestation of a qBIC resonance under oblique incidence to provide the transmission feature. For the 2D ZCG (Figure 1b), the target spectrum was a single Lorentzian transmission resonance. 1D ZCGs and square-symmetric 2D ZCGs can both be uniquely described by just four geometric degrees of freedom (DoFs), reducing the size of the parameter space that needed to be explored. We utilized a heuristic particle swarm optimization (PSO) algorithm to produce designs with the desired narrowband transmission features and sideband extinction. Simulated spectra of n ZCGs defined by a swarm of n distinct parameter sets $\mathbf{x}_{i,1\to n}$ were used to calculate figures of merit $F(\mathbf{x}_{i,1\to n})$. These figures of merit inform perturbations to each parameter set that generate the $\mathbf{x}_{i+1,1\to n}$ used in the next iteration of the optimizer. These perturbations are calculated such that the swarm ultimately converges on an optimized parameter set. The transmission spectra were generated from rigorous coupled wave analysis (RCWA) simulations implemented in MATLAB,[61] We added one DoF by defining the optimization waveband in terms of a free parameter. We first related the longest (λ_{max}) and shortest (λ_{min}) simulation wavelengths via a fixed quantity that we termed the "ratio bandwidth" (R_{bw}) such that $\lambda_{max} = R_{bw}\lambda_{min}$, then freed the ($\lambda_{min}$) parameter in optimization. As we used off-the-shelf silicon films, we lost a DoF by fixing the total film thickness (t). Our optimization vector therefore contained the starting wavelength, etch depth e, grating fill factor (FF) and period (Λ), i.e., $\mathbf{x} = (FF, \Lambda, e, \lambda_{min})$. The relevant structural parameters are shown in Figure 1a,b.

Silicon's TO coefficient has wavelength and temperature dependence. Therefore, in order to simulate the ZCG's MIR transmission spectra at different temperatures, we required a dataset of coefficients that covered these wavelengths and temperatures. The TO coefficient of c-Si has been measured within various wavelength and temperature regimes. For instance, Frey et al. (2006) experimentally measures the index of c-Si across the 1.1–5.5 μm IR band, but only from 30 to 295 K.[62] We employed the quasi-empirical dataset from Li et al. (1980) that fits a theoretically-derived model to experimental values from literature. This dataset spans 1.2–14 μm, and 100–750 K and only differs from the Frey et al. dataset by a mean absolute error of 0.0030 in the temperature-wavelength overlap in the two datasets.

3. Fabrication

Next, we describe the nanofabrication of the ZCGs. Our process was identical for the 1D and 2D gratings, with the obvious

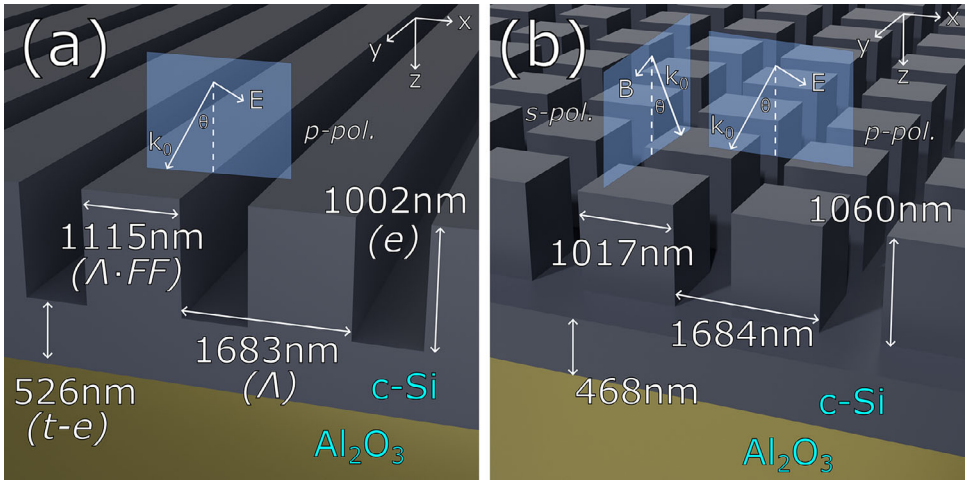

Figure 1. a) Diagram of the ideal geometries of the 1D and b) 2D ZCG, with depictions of the conventions for *s* and *p* polarized incident fields for classical incidence conditions. Naming conventions for etch depth (*e*) film thickness (*t*), fill factor (*FF*) and period Λ are also included.

exception of the patterns used in the lithography step. Our filters began as square wafer pieces of side length 12.5 mm, diced from an SoS wafer with a diameter of 4 inches. To create an etch mask (alumina, thickness: 30 nm), we employed a combination of electron beam lithography-, electron beam evaporation and liftoff. Finally, we partially etched the unmasked regions of the silicon film using inductively coupled plasma-reactive ion etching (ICP-RIE) to target depths of 1002 and 1060 nm for the 1D ZCG (Figure 1a) and 2D ZCG (Figure 1b), respectively. This etch step ultimately determined the thicknesses of both the grating and waveguide layer in the final filter. Any residual alumina from the mask layer was left on the sample after etching.

Following ICP-RIE, we imaged the etched samples with a scanning electron microscope (SEM), tilting the sample with respect to the electron beam (see **Figure** 2a,b). We could also obtain measurements of the grating heights from these images; however, we did not rely on these to provide an accurate representation of vertical geometry for several reasons. Factors that impede accurate determination of etch depth from SEM images include depth of field, resolution, electron beam aberrations, the residual alumina mask, and rounded features at the trench and grating edges. Even if these issues were not present, we would not be able to ascertain the thickness of the waveguide layer without cleaving the sample. Rather than using the SEM images to ascertain etch depth, we instead measured transmission spectra experimentally and compared them with RCWA simulations. We simulated with etch depths that increase in 10 nm intervals, and assumed the actual depth was that of the simulated structure that best matched with measurement. We then re-etched the sample based on these estimates to produce the desired transmission characteristics. For the 1D ZCG, the additional etching needed was determined to be 110 nm. For the 2D ZCG, the additional etching needed was 100 nm. This results in the samples shown in Figure 2a–d. Residual errors following this process are discussed in the Supporting Information (Figure S6).

4. Filter Characterization

We characterized the relationship between sample temperature and the transmission spectra of the 1D and 2D ZCGs using a spectroscopy setup built around a Fourier transform infrared (FTIR) spectrometer (**Figure** 3). Light from a blackbody passed through the Michelson interferometer, then exited the FTIR unit through an external port. This light passed through a wiregrid polarizer and adjustable iris, which served to polarize the incident beam, and confine the illuminating beam cross-section to within the patterned area of the ZCG. The light then passed through the ZCG, which was mounted on a temperature-controlled microscopy stage (Linkam, THMS600). The stage's rear aperture, in conjunction with the iris, effectively constrained the system's

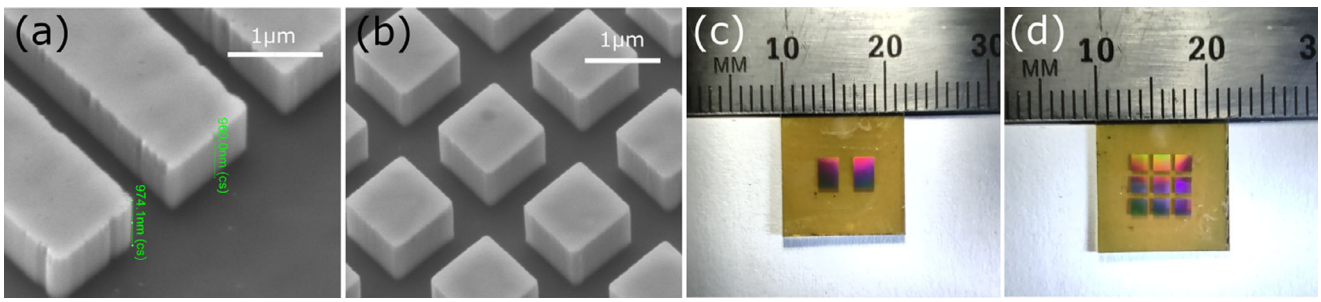

Figure 2. a) SEM image of the fabricated 1D ZCG and b) the 2D ZCG used in this experiment. c) Photographs of the fabricated 1D ZCG filter and d) 2D ZCG filter.

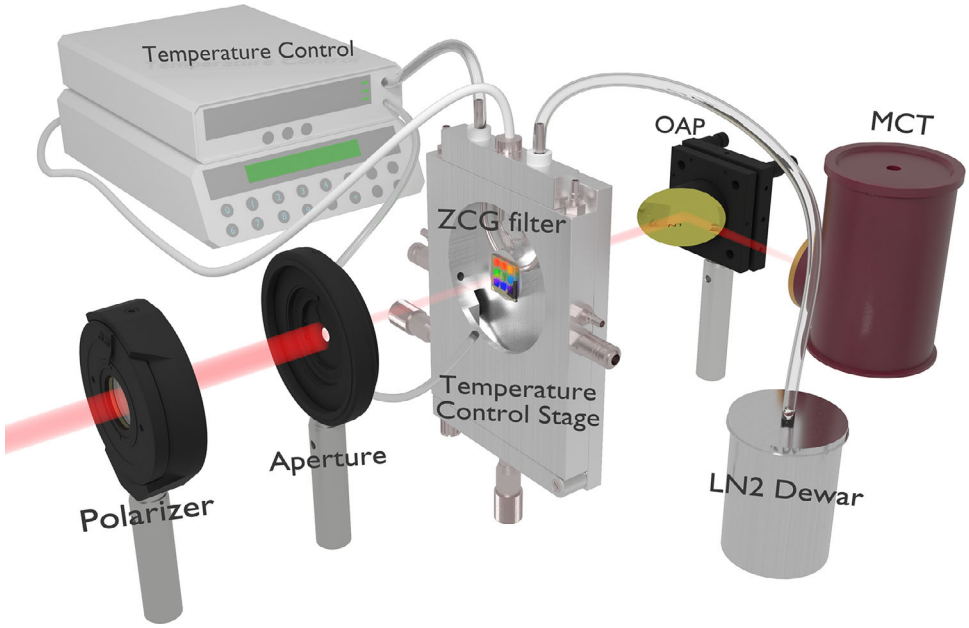

Figure 3. Render of benchtop setup used for measuring spectral transmission of the ZCG at different temperatures. Infrared light from the external port of the FTIR passed through the polarizer and iris before illuminating the metasurface. Transmitted light was then focused onto the infrared detector by an off-axis parabolic mirror.

angular aperture to only a few degrees. The light transmitted through our ZCG device was finally collected by an off-axis parabolic mirror (OAP) onto a mercury cadmium telluride detector (MCT) that provided the requisite signal to the FTIR.

For each ZCG, we programmed the stage's control module to heat the sample mount to 25 °C, 50 °C, and then to 600 °C in 50 °C increments. We waited 30 s before recording each IR power spectrum to ensure that the sample was in thermal equilibrium with the stage. After taking the final spectral measurement (at 600 °C), we allowed the ZCG to return to room temperature, removed it from the stage, and recorded a background illumination spectrum to normalize our measurements. Dividing the other IR spectra by this background spectrum provided the transmission results in **Figure** 4a,b. We employed a similar method to additionally characterize the 2D ZCG under sub-ambient conditions (−180 °C – +25 °C). The inlet port of the stage's cooling system was connected to a liquid nitrogen (LN2) dewar, and the output port to a pump whose flow rate was controlled by the temperature control module. We used this system to reduce the temperature in 50 °C increments starting at 0 °C down to −150 °C, then to a minimum of −180 °C. To minimize the formation of ice on the stage's windows, it was necessary to reduce the relative humidity of the air in their vicinity. To achieve this, we directed the gaseous nitrogen exhaust from the LN2 pump on to the front window, and hot air from a solder reflow gun on to the rear window. Despite these countermeasures, we observed a substantial reduction in peak transmission that we attribute to attenuation and scattering from water condensation.

When tuning the temperature from 25 °C to 600 °C, we measured the primary resonance redshift from 3486 nm to 3586 nm for the 1D ZCG, and 3436 nm to 3562 nm for the 2D ZCG. This work therefore demonstrates that the 1D ZCG acts as a tunable bandpass filter, with a tuning range of 100 nm as the temperature was varied from 25 to 600 °C. Similarly, over the same tempera-

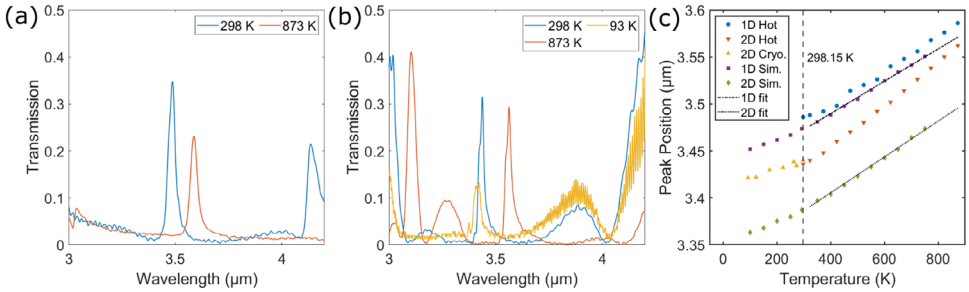

Figure 4. a) Experimentally-measured transmission spectra of 1D ZCG at room temperature (blue curve) and at 600 °C (orange curve) for p-polarized light incident at 4° from normal. b) Experimentally-measured transmission spectra of the 2D ZCG at −180 °C (yellow curve), room temperature (blue curve), and at 600 °C (orange curve) for normally-incident light. c) Position of peak of transmission spectrum versus temperature for the ZCGs under simulation (Sim.), and under experimental heating (Hot) and cooling (Cryo., 2D ZCG only).

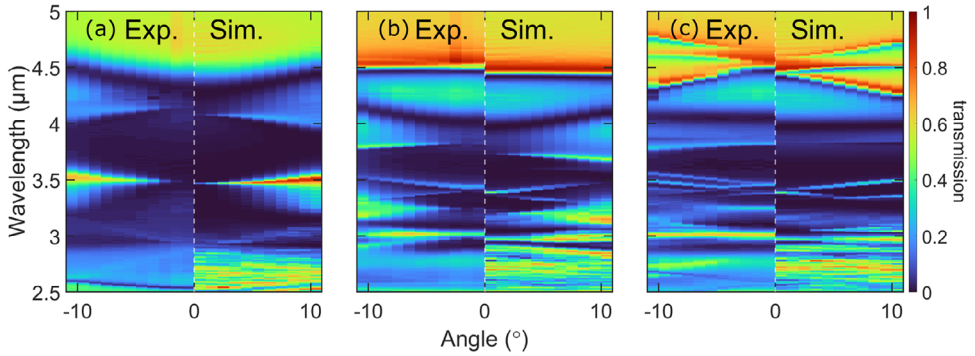

Figure 5. a) Butterflied simulation (Sim.) and experimental (Exp.) mid-infrared spectral transmission plots exhibited by the 1D and b) 2D ZCGs for p-polarized light at increasing angles of incidence for an $x-z$ plane of incidence with respect to Figure 1a,b. c) Identical conditions of the 2D ZCG as in (b) but with s-polarized light. Simulated transmission maps incorporate losses and cavity effects from the substrate, as well as a 2D Gaussian blur applied to mimic the beam divergence of the characterization setup ($\sigma_\theta = 1°$), and the resolution of the FTIR ($\sigma_\lambda = 8\ \mathrm{cm}^{-1}$).

ture range, our 2D ZCG has a tuning range of 126 nm. In the sub-ambient regime, the primary resonance of the 2D ZCG blue shifts to 3421 nm. Over the temperature range −180 °C to 600 °C, our 2D ZCG therefore has a tuning range of 141 nm. For comparison, we performed RCWA transmission simulations using the TO refractive indices from ref. [42] and plot the spectral peak positions against our measured values (Figure 4c). We observe that the total shift of 97 nm in the simulated 1D ZCG was 3 nm less than measured, and the 132 nm shift in the simulated 2D ZCG was only 9 nm less than measured.

In the 2D ZCG, at any given temperature, we observe a consistent offset between simulated and measured peak positions, which we attribute to errors in the RIE step. This offset persists in comparisons between spectral transmission measurements and simulations of the ZCGs under oblique incidence conditions (**Figure** 5b–c). We substitute the temperature control stage with a manual rotation stage, and adjust the angle of incidence in 1° increments up to a maximum of 10°. The broadening of the bandpass resonance near 3500 nm in Figure 5a in response to *p* polarized light at increasing incident angles was consistent with a symmetry protected bound-state-in-the-continuum resonance.[5] We did not explore the *s* polarized incidence of the 1D ZCG as we had only optimized for *p* polarized incidence. COMSOL Multiphysics eigenfrequency decompositions of the ZCGs are provided in the Supporting Information, with Figures S5 and S6 depicting the evolution of the eigenmode spectra with angle of incidence and temperature.

5. Reconstruction of Mid-Infrared Transmission Spectra

To demonstrate the viability of thermo-optically tuned filters for spectral analysis, we performed spectral reconstructions of the transmittance of everyday objects that have distinct features in the tuning band of the ZCGs. Our intended NDIR microspectrometer configuration would comprise an emitter, a BPF for waveband selection, a tunable ZCG filter, and a detector. The spectral transmittance of a sample inserted into the system can be algorithmically reconstructed from the varying detector signal, recorded as a function of the ZCG's temperature. We repurpose the FTIR's MCT detector and blackbody emitter to emulate such a configuration.

We noted that the MCT detector's photocurrent was proportional to the integrated product of its spectral responsivity with the spectral power density (SPD) of any incident light. For spectral data sampled at N discrete points, this integral can be approximated as a scalar product if N is sufficiently large. We encoded the sample transmittance in an $N \times 1$ vector, denoted as $\mathbf{x}$. Furthermore, we assumed all other components operated linearly, allowing us to encode the system's optical response, multiplexed at M discrete temperatures in an $M \times N$ matrix, which we denoted by A. This allowed us to approximate the MCT photocurrent at these M discrete temperatures as the product $A \cdot \mathbf{x}$, given by the vector $\mathbf{y}$. We accounted for the inevitable presence of noise by adding the vector $\mathbf{y}_{\mathrm{noise}}$ to yield Equation (1), which models the MCT signals in terms of the system's optical response, the transmission spectrum of the unknown sample, and any noise contributions.

$$\mathbf{y} = A \cdot \mathbf{x} + \mathbf{y}_{\mathrm{noise}} \tag{1}$$

If the number of spectral data points exceeds the number of temperature data points, i.e., $M < N$, Equation (1) is underdetermined. Additionally, detector noise prohibits solvers from precisely determining the spectrum, even for an overdetermined system (i.e., $M \geq N$). Therefore, we used an off-the-shelf linear solver to perform the reconstruction, specifically, the recursive least-squares (RLS) adaptive filtering algorithm. Constraints can be introduced to this iterative solver that encourage physically reasonable solution spectra. For example, the solution vector may be forced to be positive after each iteration, or a regularization parameter may be included to discourage sparse solutions.[63]

We modified the setup of Figure 3 to include an off-the-shelf, broadband BPF (THORLABS, FB3500-500) which has cut-on and cutoff wavelengths of 3250 and 3750 nm respectively. This broadband BPF filtered out emission from the FTIR's internal blackbody outside the working band of the 2D ZCG. We tested the reconstruction capability of our thermal tuning method using a variety of samples drawn from our laboratory that possessed distinctive MIR transmission features. These comprised low den-

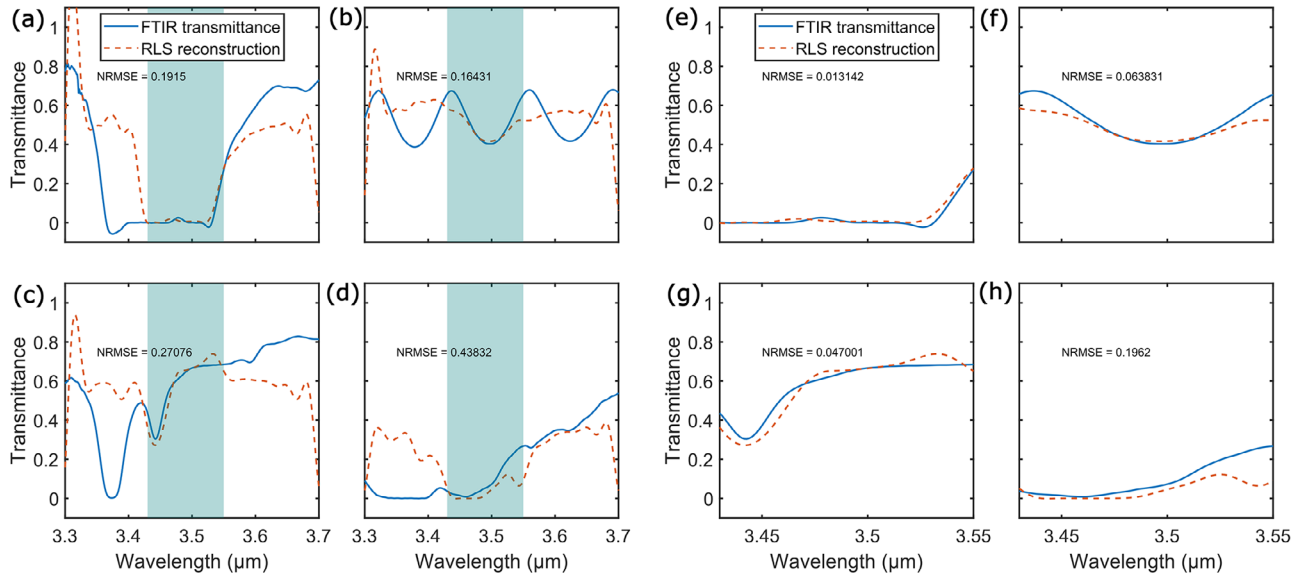

Figure 6. Broadband reconstructed spectra for a) low density polyethylene b) an empty liquid cell with zinc selenide windows c) polymide tape, and d) polyethylene terephthalate. The shaded regions indicate the passband tuning exhibited by the 2D ZCG over the 25 °C to 420 °C thermal range. e–h) depict the same spectra from (a–d), but constrained to the shaded regions of 3430–3550 nm.

sity polyethylene (LDPE) in the form of a ziplock bag, an empty liquid cell with zinc selenide windows (Specac, Omnicell), polyimide (Kapton) tape, and polyethylene terephthalate in the form of plastic clamshell packaging.

We utilized a thermal stage to heat the ZCG in 25 °C increments from 25 °C to 400 °C then finally to 420 °C, providing $M = 17$ discrete temperatures. This stage (Linkam, LTS420) was similar to the stage in the earlier parts of the paper (Linkam, THMS600). We measured the ZCG transmission spectrum at each temperature to produce the rows of the A matrix. In turn, the entries of the $\mathbf{y}$ signal vector could be obtained by integrating the FTIR's measured SPD with the sample present at each temperature. In our intended, microspectrometer configuration, A would only need to be measured once, while $\mathbf{y}$ would be read directly from the photodetector signal. These matrices served as the inputs to our RLS algorithm that produced a solution vector $\mathbf{x}$ that best satisfied Equation 1. The results are shown as **Figure 6**a–d. It can be seen that the fidelity of the reconstructions ($\mathbf{y}_{\text{recon}}$, dotted red lines) with respect to the FTIR-measured ground truth ($\mathbf{y}_{\text{true}}$, blue solid lines) were observed to excel within the spectral region through which the ZCG's passband can be tuned with temperature (blue shaded region). These regions are re-plotted in Figure 6e–h. In the case of LDPE, a normalized root-mean-square error of 0.013 between reconstructed and true transmittance was achieved. This was determined using Equation (2).

$$\text{NRMSE}(\mathbf{y}_{\text{recon}}, \mathbf{y}_{\text{true}}) = \frac{1}{\bar{\mathbf{y}}_{\text{true}}} \sqrt{\sum_{i}^{n} \frac{(\mathbf{y}_{\text{recon},i} - \mathbf{y}_{\text{true},i})^2}{n}} \tag{2}$$

In theory, the ZCG and thermal stage will contribute blackbody thermal emission with increasing temperature. However, the FTIR spectrometer utilizes the Fourier transform of the MCT photocurrent with respect to the modulation of the internal interferometer; any unmodulated emission sources manifest as a DC signal that is filtered out by the system. In our intended use-case (compact mid-IR spectrometer comprising a broadband source, BPF, tunable ZCG and detector), equivalent background signal filtering could be achieved by chopping the incident light and measuring only the modulated signal. Alternatively, a temperature-dependent background could be recorded prior to measurement with the sample present.

6. Conclusion

Using the thermo-optic coefficient of silicon, we demonstrate tuning of the spectral resonances of a pair of silicon-on-sapphire ZCGs. Tuning ranges of 100 nm and 141 nm are measured for the 1D ZCG (from 25 °C to 600 °C) and the 2D ZCG (from −180 °C to 600 °C), respectively. These ranges exceed the respective 25 nm and 29 nm full-width-at-half-maximum (FWHM) values of the resonances, meaning that the peaks are completely resolved. The thermal and angular tuning characteristics of the bandpass resonances in our fabricated 1D and 2D ZCGs are also consistent with simulations.

We apply this tuning capability to the spectral reconstruction of the transmission spectra of several samples with distinctive mid-infrared spectra. We observed reasonable agreement between the reconstructed and ground truth spectra in all samples after a single acquisition and were able to achieve a normalized root-mean-square error of 0.013 in the case of a low density polyethylene sample across the 3430 to 3550 nm spectral band.

To minimize the filtering systems physical footprint, power consumption, and excess emission, the commercial heating stage (Linkam) would need to be replaced with an integrated microheater system. This would permit repeatable and rapid tuning, e.g., as seen in ref. [40]. We could achieve this using electrically resistive materials such as indium tin oxide in an internal layer, or by introducing graphene as a 2D top layer as in ref. [23].

Supporting Information

Supporting Information is available from the Wiley Online Library or from the author.

Acknowledgements

This work was performed in part at the Melbourne Centre for Nanofabrication (MCN) in the Victorian Node of the Australian National Fabrication Facility (ANFF). This work was supported in part by the MCN Technology Fellow Ambassador program. This work was supported in part by the Australian Research Council Centre of Excellence for Transformative Meta-Optical Systems (Project No. CE200100010). The authors gratefully acknowledge Dr. James Hutchison and Prof. Trevor Smith for the use of equipment.

Conflict of Interest

The authors declare no conflict of interest.

Data Availability Statement

The data that support the findings of this study are available from the corresponding author upon reasonable request.

Keywords

dielectric gratings, infrared filtering, metasurfaces

Received: June 8, 2024
Revised: April 29, 2025
Published online: June 12, 2025

[1] A. Lochbaum, A. Dorodnyy, U. Koch, S. M. Koepfli, S. Volk, Y. Fedoryshyn, V. Wood, J. Leuthold, *Nano Lett.* **2020**, *20*, 4169.
[2] W. Ye, Z. Tu, X. Xiao, A. Simeone, J. Yan, T. Wu, F. Wu, C. Zheng, F. K. Tittel, *Sensors* **2020**, *20*, 5461.
[3] B. J. Russell, J. Meng, K. B. Crozier, *IEEE Sens. J.* **2023**, *23*, 22389.
[4] J. Meng, L. Weston, S. Balendhran, D. Wen, J. J. Cadusch, R. R. Unnithan, K. B. Crozier, *Laser and Photonics Reviews* **2022**, 2100436.
[5] B. J. Russell, J. J. Cadusch, J. Meng, D. Wen, K. B. Crozier, *Opt. Lett.* **2022**, *47*, 2490.
[6] S. Zhang, Y. Dong, H. Fu, S. L. Huang, L. Zhang, *Sensors (Switzerland)* **2018**, *18*.
[7] B. J. Craig, J. Meng, V. R. Shrestha, J. J. Cadusch, K. B. Crozier, *Sci. Rep.* **2019**, *9*, 1.
[8] S. Yasunaga, T. Kan, *Opt. Express* **2022**, *30*, 20820.
[9] K. Chen, S. Liu, B. Zhang, Z. Gong, Y. Chen, M. Zhang, H. Deng, M. Guo, F. Ma, F. Zhu, Q. Yu, *Opt. Lasers Eng.* **2020**, *124*, 105844.
[10] J. Meng, J. J. Cadusch, K. B. Crozier, *ACS Photonics* **2021**, *8*, 648.
[11] A. Emadi, H. Wu, G. de Graaf, R. Wolffenbuttel, *Opt. Express* **2011**, *20*, 489.
[12] T. Jeon, A. Nateghi, W. M. Jones, C. Choi, J. P. Cardenas, C. Ross, A. Scherer, *ACS Photonics* **2022**, *9*, 68.
[13] H. Mao, D. K. Tripathi, Y. Ren, K. K. M. B. D. Silva, M. Martyniuk, J. Antoszewski, J. Bumgarner, J. M. Dell, L. Faraone, *IEEE J. Sel. Top. Quantum Electron.* **2017**, *23*, 45.
[14] D. K. Tripathi, H. Kala, K. K. M. B. D. Silva, M. Martyniuk, G. Putrino, B. Nener, L. Faraone, in *2018 Conference on Optoelectronic and Microelectronic Materials and Devices (COMMAD)*. IEEE, ISBN 9781538695241, **2018**.
[15] A. Leitis, A. Tittl, M. Liu, B. H. Lee, M. B. Gu, Y. S. Kivshar, H. Altug, *Sci. Adv.* **2019**, *5*, 1.
[16] G. Hu, A. Krasnok, Y. Mazor, C.-W. Qiu, A. Alù, *Nano Lett.* **2020**, *20*, 3217.
[17] K. Iwami, C. Ogawa, T. Nagase, S. Ikezawa, *Opt. Express* **2020**, *28*, 35602.
[18] H.-S. Ee, R. Agarwal, *Nano Lett.* **2016**, *16*, 2818.
[19] S. Wei, G. Cao, H. Lin, X. Yuan, M. Somekh, B. Jia, *ACS Nano* **2021**, *15*, 4769.
[20] C. U. Hail, A.-K. U. Michel, D. Poulikakos, H. Eghlidi, *Adv. Opt. Mater.* **2019**, *7*, 1801786.
[21] Y. Che, X. Wang, Q. Song, Y. Zhu, S. Xiao, *Nanophotonics* **2020**, *9*, 4407.
[22] C. Zou, C. Amaya, S. Fasold, A. A. Muravsky, A. A. Murauski, T. Pertsch, I. Staude, *ACS Photonics* **2021**, *8*, 1775.
[23] A. Nagpal, M. Zhou, O. Ilic, Z. Yu, H. A. Atwater, *Opt. Express* **2023**, *31*, 11227.
[24] M. Li, S. Biswas, C. U. Hail, H. A. Atwater, *Nano Lett.* **2021**, *21*, 7602.
[25] A. Forouzmand, M. M. Salary, G. K. Shirmanesh, R. Sokhoyan, H. A. Atwater, H. Mosallaei, *Nanophotonics* **2019**, *8*, 415.
[26] P. C. Wu, R. Sokhoyan, G. K. Shirmanesh, W.-H. Cheng, H. A. Atwater, *Adv. Opt. Mater.* **2021**, *9*, 2100230.
[27] S. Abdollahramezani, O. Hemmatyar, M. Taghinejad, H. Taghinejad, A. Krasnok, A. A. Eftekhar, C. Teichrib, S. Deshmukh, M. A. El-Sayed, E. Pop, M. Wuttig, A. Alù, W. Cai, A. Adibi, *Nat. Commun.* **2022**, *13*, 1696.
[28] K. Z. Kamali, L. Xu, J. Ward, K. Wang, G. Li, A. E. Miroshnichenko, D. Neshev, M. Rahmani, *Small* **2019**, *15*, 1805142.
[29] T. Lewi, N. A. Butakov, J. A. Schuller, *Nanophotonics* **2018**, *8*, 331.
[30] M. Celebrano, D. Rocco, M. Gandolfi, A. Zilli, F. Rusconi, A. Tognazzi, A. Mazzanti, L. Ghirardini, E. A. A. Pogna, L. Carletti, C. Baratto, G. Marino, C. Gigli, P. Biagioni, L. Duò, G. Cerullo, G. Leo, G. D. Valle, M. Finazzi, C. D. Angelis, *Opt. Lett.* **2021**, *46*, 2453.
[31] D. C. Zografopoulos, V. Dmitriev, *J. Lightwave Technol.* **2021**, *39*, 6985.
[32] T. V. Tsoulos, G. Tagliabue, *Nanophotonics* **2020**, *9*, 3849.
[33] M. Bosch, M. R. Shcherbakov, Z. Fan, G. Shvets, *J. Appl. Phys.* **2019**, *126*, 073102.
[34] H. Kocer, A. Ozer, S. Butun, K. Wang, J. Wu, H. Kurt, K. Aydin, *IEEE J. Sel. Top. Quantum Electron.* **2019**, *25*, 1.
[35] C. Luo, D. Li, J. Yao, F. Ling, *J. Electromagn. Waves Appl.* **2015**, *29*, 2512.
[36] T. Cui, B. Bai, H.-B. Sun, *Adv. Funct. Mater.* **2019**, *29*, 1806692.
[37] T. Xu, E. C. Walter, A. Agrawal, C. Bohn, J. Velmurugan, W. Zhu, H. J. Lezec, A. A. Talin, *Nat. Commun.* **2016**, *7*, 1.
[38] C. Williams, N. Hong, M. Julian, S. Borg, H. J. Kim, *Opt. Express* **2020**, *28*, 10583.
[39] M. N. Julian, C. Williams, S. Borg, S. Bartram, H. J. Kim, *Optica* **2020**, *7*, 746.
[40] K. Z. Kamali, L. Xu, N. Gagrani, H. H. Tan, C. Jagadish, A. Miroshnichenko, D. Neshev, M. Rahmani, *Light: Sci. Appl.* **2023**, *12*, 40.
[41] M. J. Uddin, R. Magnusson, *IEEE Photonics Technol. Lett.* **2013**, *25*, 1412.
[42] H. H. Li, *J. Phys. Chem. Ref. Data* **1980**, *9*, 561.
[43] K. Nishida, K. Sasai, R. Xu, T.-H. Yen, Y.-L. Tang, J. Takahara, S.-W. Chu, *Nanophotonics* **2022**, *12*, 139.
[44] K. Nishida, H.-Y. Cheng, M. Petrov, K.-P. Chen, J. Takahara, X. Li, K.-H. Lin, S.-W. Chu, *J. Opt. Soc. Am. B* **2024**, *41*, D61.
[45] T. Lewi, H. A. Evans, N. A. Butakov, J. A. Schuller, *Nano Lett.* **2017**, *17*, 3940.
[46] L. Macé, O. Gauthier-Lafaye, A. Monmayrant, H. Camon, B. Portier, in *2017 European Conference on Lasers and Electro-Optics and European Quantum Electronics Conference*, **2017**.

[47] L. Macé, O. Gauthier-Lafaye, A. Monmayrant, S. Calvez, H. Camon, H. Leplan, *AIP Adv.* **2018**, *8*, 115228.
[48] Y. H. Ko, R. Magnusson, *Opt. Lett.* **2016**, *41*, 4704.
[49] Y. Ding, R. Magnusson, *Opt. Lett.* **2004**, *29*, 1135.
[50] M. Barrow, M. Scherr, J. Phillips, *IEEE Photonics J.* **2018**, *10*, 1.
[51] A. S. L. Krishna, S. Menon, A. Prosad, V. Raghunathan, *Photonics Res.* **2021**, *10*, 68.
[52] Y. H. Ko, M. Niraula, R. Magnusson, *Opt. Lett.* **2016**, *41*, 3305.
[53] Y. Chai, G. Kang, *Appl. Opt.* **2022**, *61*, 8819.
[54] G. Quaranta, G. Basset, O. J. F. Martin, B. Gallinet, *Laser and Photonics Reviews* **2018**, *12*, 1.
[55] R. Magnusson, *Opt. Lett.* **2014**, *39*, 4337.
[56] D. A. Bykov, E. A. Bezus, L. L. Doskolovich, *Phys. Rev. A* **2019**, *99*, 063805.
[57] M. Niraula, J. W. Yoon, R. Magnusson, *Opt. Express* **2014**, *22*, 25817.
[58] S. Z. Cohen, D. Singh, S. Nandi, T. Lewi, *Nanophotonics* **2023**, *12*, 3217.
[59] D. G. Cahill, S.-M. Lee, T. I. Selinder, *J. Appl. Phys.* **1998**, *83*, 5783.
[60] University wafer, silicon on sapphire (SoS) wafers, https://www.universitywafer.com/silicon-on-sapphire.html.
[61] S. Zanotto, Ppml - periodically patterned multilayer, **2022**, https://au.mathworks.com/matlabcentral/fileexchange/55401-ppml-periodically-patterned-multi-layer.
[62] B. J. Frey, D. B. Leviton, T. J. Madison, In E. Atad-Ettedgui, J. Antebi, D. Lemke, editors, *SPIE Proceedings*. SPIE, **2006**.
[63] C. Paleologu, J. Benesty, C. Stanciu, C. Anghel, M. Stenta, in *2016 8th International Conference on Electronics, Computers and Artificial Intelligence (ECAI)*. IEEE, **2016**, pp. 1–4.